

 Open access • Journal Article • DOI:10.1039/C6AN00169F

More from less: high-throughput dual polarity lipid imaging of biological tissues.

— [Source link](#) 

Shane R. Ellis, Joanna Cappell, Nina Ogrinc Potočnik, Benjamin Balluff ...+3 more authors





Institutions: Maastricht University, University of Antwerp

Published on: 07 Jun 2016 - Analyst (The Royal Society of Chemistry)

Topics: Zebra finch and Mass spectrometry imaging

Related papers:

- [Sublimation of New Matrix Candidates for High Spatial Resolution Imaging Mass Spectrometry of Lipids: Enhanced Information in Both Positive and Negative Polarities after 1,5-Diaminonaphthalene Deposition](#)
- [Use of advantageous, volatile matrices enabled by next-generation high-speed matrix-assisted laser desorption/ionization time-of-flight imaging employing a scanning laser beam](#)
- [Imaging mass spectrometry](#)
- [MALDI imaging of lipid biochemistry in tissues by mass spectrometry.](#)
- [Desorption electrospray ionization then MALDI mass spectrometry imaging of lipid and protein distributions in single tissue sections.](#)

Share this paper:    

View more about this paper here: <https://typeset.io/papers/more-from-less-high-throughput-dual-polarity-lipid-imaging-jqpvyoawi>

This item is the archived peer-reviewed author-version of:

More from less : high-throughput dual polarity lipid imaging of biological tissues

Reference:

Ellis Shane R., Cappell Joanna, Potocnik Nina Ogrinc, Balluff Benjamin, Hamaide Julie, Van Der Linden Anne-Marie, Heeren Ron M. A..- More from less : high-throughput dual polarity lipid imaging of biological tissues
The analyst - ISSN 0003-2654 - 141:12(2016), p. 3832-3841
Full text (Publishers DOI): <http://dx.doi.org/doi:10.1039/C6AN00169F>
To cite this reference: <http://hdl.handle.net/10067/1346580151162165141>

More From Less: High-Throughput Dual Polarity Lipid Imaging of Biological Tissues

Shane R. Ellis^{1*}, Jo Cappell¹, Nina Ogrinc Potočnik¹, Benjamin Balluff¹, Julie Hamaide²,
Annemie Van Der Linden² and Ron M. A. Heeren¹

¹ M4I, The Maastricht Multimodal Molecular Imaging Institute, 6229 ER Maastricht, The Netherlands

² Bio-Imaging Lab, University of Antwerp, 2610 Wilrijk, Belgium

* Corresponding Author

s.ellis@maastrichtuniversity.nl

Abstract

The high ion signals produced by many lipids in mass spectrometry imaging make them an ideal molecular class to study compositional changes throughout tissue sections and their relationship with disease. However, the large extent of structural diversity observed in the lipidome means optimal ion signal for different lipid classes is obtained in opposite polarities. In this work we demonstrate how new high speed MALDI-MSI technologies, combined with precise laser position control enables the acquisition of positive and negative ion mode lipid data from the same tissue section much faster than is possible with other MSI instruments. Critically, using this approach, we explicitly demonstrate how such dual polarity acquisitions provide more information regarding molecular composition and spatial distributions throughout biological tissues. For example, in applying this approach to the zebrafish songbird brain we reveal the high abundance of DHA containing phospholipids (PC in positive mode and PE, PS in negative ion mode) in the nuclei that control song learning behaviour. To make the most of dual polarity data from single tissues we also have developed a pLSA-based multivariate analysis technique that includes both positive and negative ion data in the classification approach. In doing so the correlation amongst different lipid classes that ionise best in opposite polarities and contribute to certain spatial patterns within the tissue can be directly revealed. To demonstrate we apply this approach to studying the lipidomic changes throughout the tumor microenvironment within xenografts from a lung cancer model.

Introduction

Our knowledge of the lipidome within tissues and cells has increased dramatically over the last 10-15 years.¹⁻⁴ In no small part this has been driven by developments of mass spectrometry-based lipidomics methods enabling molecular-level lipid analysis from biological extracts.⁵ In parallel with these developments the field of mass spectrometry imaging (MSI) has emerged as a powerful complimentary technique allowing the spatial localisation of multiple molecular lipids within tissues and cells to be studied simultaneously.⁶⁻¹⁰ These approaches, spanning many ionisation techniques but in particular matrix-assisted laser desorption ionisation (MALDI), secondary ion mass spectrometry (SIMS) and desorption electrospray ionisation (DESI) have provided powerful tools for understanding how the lipid composition of tissues changes within different tissue types and sub-types. One key application of this has been to use the localised changes in lipid profiles to readily distinguish and chemically characterise different tissue regions, such as those encountered in tumors.^{7, 11-17}

Despite lipids producing typically abundant signals in MSI experiments, a comprehensive molecular coverage requires tissues be analysed in both positive and negative mode. The vast structural diversity of lipids results in preferential ionisation of certain lipid classes in a single polarity. For example zwitterionic PCs and sphingomyelins, along with neutral lipids such as triacylglycerols are observed almost exclusively in positive ion mode while other phospholipids such as PI, PS, PE and PGs in addition to many sialyated glycosphingolipids and cardiolipins are observed much more efficiently in negative ion mode. With MALDI, the most common approach for lipid MSI, there are two possibilities to approach dual-polarity acquisitions. The first is to perform each experiment on adjacent tissue sections using optimised matrices for each polarity. For example, such an approach has been demonstrated for the metabolites and lipid imaging of corn seeds¹⁸ and for tumor tissue.¹⁹ The second

approach is to acquire both polarities from the same tissues section. This is advantageous as it allows direct correlation of positive and negative data on the same tissue without the need to correct for small alignment problems arising from deformations during sectioning and for small histological changes between adjacent sections. Moreover, it makes most efficient use of precious tissues, such as those from biopsies. Several recent studies have demonstrated this approach using rapid polarity switching from pixel-to-pixel however this approach is not available on all instrument platforms.^{20, 21} Alternatively, using MALDI matrices that produce efficient ionisation in both polarities (for example DAN,²² dithranol and DHAP²³) one polarity can be acquired with sufficient gaps left between the analysed areas which are then used for acquisition of the second polarity sequentially with an appropriate stage offset.^{22, 24} However, time is an important consideration of acquisitions in general and dual-polarity acquisitions take twice as long as a single polarity acquisition acquired with the same resolution. This can become a limiting factor (for example in the analysis of large tissue cohorts). The highest achievable spatial resolution is also lowered by a factor of 2.

Recently we have demonstrated that the use of new, high-speed MALDI-MSI instrumentation using a self-scanning laser beam facilitates the extremely high throughput acquisition of dual-polarity lipid MSI data at high spatial resolutions over 20-50 times faster than other MALDI-MSI systems.²³ Here we demonstrate this technique can be used to extract more molecular information and spatial patterns from tissue sections on rapid time scales. We demonstrate its use for comprehensive, high-throughput dual polarity lipid MSI of multiple tumors to investigate the lipidomics changes within the tumor microenvironment and also within the brain of the zebra finch songbird. Using multivariate image segmentation of the high dimensional dual-polarity data we show that dual polarity MSI reveals more tissue-specific features than a single polarity alone. Moreover by combining both datasets into a single

multivariate analysis model, underlying spatial correlation of many lipids classes can be directly revealed.

Experimental Methods

Materials

Methanol was purchased from Biosolve BV (Valkenswaard, The Netherlands). Chloroform (anhydrous, $\geq 99\%$), Ethanol and norharmane matrix were purchased from Sigma Aldrich (Zwijndrecht, The Netherlands). Indium tin oxide (ITO) coated glass slides were purchased from Delta Electronics (Loveland, CO, USA, 4–8 Ω/sq).

Tissue Collection and Preparation

Frozen mouse xenograft material from human cancer cell line NCI-H460 was received from AstraZeneca, UK and stored at $-80\text{ }^{\circ}\text{C}$. Sections of $7\text{ }\mu\text{m}$ were taken from four xenografts at $-18\text{ }^{\circ}\text{C}$ on a Cryostat HM525 (Microm, Walldorf, Germany) and thaw mounted onto ITO coated glass slides previously cleaned in hexane and ethanol (10 minutes each) and dried under vacuum. Fresh frozen adult male zebra finch (*Taeniopygia guttata*) brain (120 days post hatching) was sectioned into $12\text{ }\mu\text{m}$ sagittal sections and thaw mounted on conductive ITO slides. Norharmane matrix was applied to sections at 7 mg/ml in 2:1 chloroform:methanol (v/v) using a SunCollect automatic pneumatic sprayer (Sunchrom GmbH, Friedrichsdorf, Germany).

Data Acquisition

All data was acquired on a Bruker RapifleX MALDI TissueTyper™ system operating in reflectron mode (Bruker Daltonik GmbH, Bremen, Germany) with a nominal acceleration potential of ± 20 kV. MSI data was acquired using a $50 \times 50 \mu\text{m}^2$ raster and a $20 \times 20 \mu\text{m}^2$ beam scan area for each polarity with 200 laser shots accumulated at each pixel. The average acquisition rate was 23 pixels/sec. Following acquisition of negative ion data, the instrument was switched to positive ion mode and data acquired using the same coordinates but with a 25 μm stage offset. The total size of the tumor and zebrafish brain datasets was 181,278 and 80,226 pixels respectively. For further analysis data was exported as imzML files.²⁵ MS/MS spectra were acquired from adjacent tissues using on a Waters Synapt G2SI HDMS mass spectrometer (Waters, Manchester, UK). Time-of-flight calibration was performed using red phosphorous clusters in both positive and negative ion modes. All images are normalised to the total ion count.

Tissue Staining

For the tumor samples after MSI the matrix was washed off using 3 x 30 second submersions into EtOH. Tissue was rehydrated in 96% EtOH, 70% EtOH, 35% EtOH and dH₂O, 2 minutes each. The slide was placed in haematoxylin (Merck, Darmstadt, Germany) for 2 minutes, removed and washed in running tap water for 4 minutes. The slide wash then counterstained in eosin (JT Baker, Center Vally, PA, USA) for 40 seconds and washed in running tap water for 1 minute. The slide was finally washed in 100% EtOH for 2 minutes and dehydrated in xylene for 30 seconds.

For zebra finch tissue staining the sections were washed for 1 min in EtOH to remove the residual matrix. The tissue was subsequently dipped for 2 min in different EtOH solutions

(96%, 70%, dH₂O). After re-hydration the sections were placed in 0.1% cresyl violet solution (Merck, Darmstadt, Germany) in an oven at 60°C. The stained sections were washed for 2 min in dH₂O, dipped in 100% EtOH and dehydrated in xylene for 30s. After staining optical images were acquired using a MIRAX Desk scanner (Zeiss, Gottingen, Germany).

Multivariate Data Analysis

The imzML files of both polarities were read separately into the Matlab (v. R2015a) environment. Peak picking was done on the baseline subtracted and smoothed average spectrum. Smoothing was performed using the *mslowess* function (Bioinformatics Toolbox) with Gaussian kernel, order 0 and a 5 data points span width and the baseline was subtracted using the *imtophat* function (Image Processing Toolbox) with a window size calculated as the dataset individual bin size * 1E4. Peaks were picked with the *mspeaks* function (Bioinformatics Toolbox) with a relative intensity threshold compared to the basepeak of 0.5% for the zebrafinch brain datasets and 1% for the tumor dataset. The peak lists were then used to reduce the datasets by extracting the total-ion-count normalized intensities for each peak from each spectrum (pixel). Multivariate analysis was performed on the single polarity datasets first and then on the combined (dual) polarity datasets using the probabilistic latent semantic analysis (pLSA).²⁶ Combined datasets of both polarities were created by simple concatenation of negative and positive polarity datasets in the feature dimension.

Results and Discussion

Data Acquisition Approach

The precise laser control afforded by the employed MALDI instrument facilitated efficient dual polarity data acquisition using the stage offset approach. Figure 1a shows optical images of norharmane matrix deposited onto an ITO slide following MSI using a laser scan of $20 \times 20 \mu\text{m}^2$ and a raster width of $50 \times 50 \mu\text{m}^2$. Well-defined square ablation regions $\sim 20 \times 20 \mu\text{m}^2$ within each raster position are observed. The corresponding image acquired following a second acquisition with a $25 \mu\text{m}$ stage offset in the x and y directions, is shown in Figure 1b. Here it is clearly observed the second dataset is acquired from previously unablated areas in between the previous analysed regions. It should be noted that this approach has still only irradiated less than half of the sample. The remaining areas could be used, for example for MS/MS or high mass resolution data acquisitions, further enhancing the information acquired from a single tissue section.

Figures 1 c and d shows the corresponding positive and negative ion spectra from a zebra finch brain using the approach described above and norharmane matrix. Strong, complimentary lipid signals are clearly observed with virtually no lipid overlap across both polarities. In the negative ion mode strong lipid signals are observed for many lipid classes including PE, PS, PI and ST while at higher masses gangliosides were also be observed (data not shown). In positive mode PCs and several SM lipids are observed with the protonated ions being significantly more abundant than the corresponding sodiated and potassiated ions that are often found to be the dominant ion formed upon direct tissue analysis.

Having demonstrated the rapid and sensitive acquisition of lipids in positive and negative ion mode with $50 \mu\text{m}$ pixel sizes, we have investigated below the added value of dual polarity

acquisitions for better understanding and visualisation of local lipidomics changes within the zebra finch songbird brain and the tumor microenvironment.

Lipid Imaging of the Zebra finch Songbird Brain

The neuronal processes associated with song learning of songbirds provide an interesting opportunity to study their influence on behaviour and learning. The avian forebrain of the songbirds is interconnected with discrete nuclei which control the song learning behaviour. During the song learning phases these nuclei undergo a series of anatomical, neurochemical and molecular changes.²⁷ The song nuclei are interconnected in a way that they form two different pathways. The anterior forebrain pathway or the sensory pathway receives the signal at the HVC (Higher vocal center) and projects it to the striatal nucleus AreaX. The pathway continues through the dorsomedial division of the medial thalamus - DLM towards the lateral portion of the magnocellular nucleus of the anterior neostriatum (LMAN) reaching the robust nucleus of the archistriatum (RA). A subsequent interconnection from the LMAN to AreaX provides an additional signal interchange in the anterior forebrain pathway.²⁷ The caudal motor pathway forms a direct connection between HVC and RA and is responsible for the motoric aspect of singing. Several studies have provided evidence for the critical roles of lipids in the song learning process.²⁸⁻³¹ While SIMS has been used to study the distribution of fatty acids (mostly as fragments of larger lipids) within zebra finch brain tissue,^{32, 33} due to the extensive fragmentation induced by SIMS the distribution of intact molecular-lipids has not been reported. Here we have employed dual-polarity imaging to study the distribution of intact lipids within the zebra finch brain with an emphasis on the composition and distribution of specific lipid compounds in the discrete nuclei and the neuronal connections.

The average positive and negative ion spectra acquired from the tissue are shown in Figure 1. Both the positive and negative ion data sets were subjected to multivariate analysis, the complete results of which are provided in the Supporting Information Figures S1 and S2). Positive ion component 4 (Figure 2b) is strongly correlated with the Area X and RA nuclei and the ipsilateral optic tectum (TeO). The loading plot of positive ion component 4 (Figure 2c) revealed the strongest contributions towards this component arising from m/z 734.5, 760.6, 806.6 and 834.6. While the single ion images of m/z 734.5 and 760.6, identified as the $[M+H]^+$ ions of PC (32:0) and PC(34:1), were relatively homogeneously distributed throughout the tissue (data not shown), lipid ions at m/z 806.6 and m/z 834.6 (Figure 2d and e) revealed much more specific enrichment in Area X, RA and TeO and partly LMAN upon comparing their ion distributions with the annotated cresyl violet stained section. The MS/MS spectrum of m/z 806 yielded an abundant fragment ion at m/z 184 with no neutral losses arising from the phosphocholine headgroup, suggesting the presence of a protonated PC (MS/MS spectra are provided as Supporting Information Figure S3 and S4). Low abundance ions were also observed at m/z 478 and 496 and assigned to the neutral loss of a 22:6 fatty acid and ketene, and m/z 550 and 568 assigned as the analogous neutral losses from a 16:0 fatty acid. The ion at m/z 834.5 yielded analogous low abundance fragment ions allowing the assignment of a 22:6 and an 18:0 fatty acid. Based on the preferred regioselectivity of polyunsaturated fatty acids to the *sn*2 position of the glycerol backbone, these lipids can be tentatively assigned as protonated PC (16:0/22:6) and PC (18:0/22:6). These results are consistent with earlier SIMS data providing evidence for the enrichment of 22:6 (DHA) fatty acids in the RA and LMAN regions region³³ and provide the first molecular lipid localisation in the zebra finch brain, however significant enrichment of 22:6 in Area X was not observed by SIMS. One possible explanation is that the tissues may have been taken from different locations throughout the volume of the brain containing AreaX and the molecular composition may change with depth

thought the brain. Interestingly in the negative ion pLSA analysis the assignment of a spectral distribution correlating specifically with AreaX, RA and TeO was less pronounced. Examination of the negative mode single m/z images that did show some correlation with these regions (Negative components 2 and 8) revealed the localisation of further DHA containing phospholipids in AreaX, RA and TeO (Supporting Information Figure S5). For example, m/z 774 produced specific fragment ions upon MS/MS corresponding to the presence of a 22:6 fatty acid and can thus be assigned as $[\text{PE}(\text{p-18:0}/22:6)\text{-H}]^-$. Based on these results, those of Amaya *et al.*³² and the known importance of DHA in brain development and function³⁴⁻³⁸ it appears DHA containing lipid plays an important role in the songbird control and learning circuitry.

In the negative ion mode (Component 3, Figure 2f) the laminae that partition the brain in different subareas can be observed. These laminae are not as strongly observed in the positive ion pLSA analysis. The loadings spectrum for negative component 3 reveals strong correlations between m/z 904.6, 888.6, 862.6 and 806.6 and the component 3 image. The dominant lipids contributing to these signals were identified via MS/MS (see Supporting Information Figure S4) as $[\text{ST}(\text{d18:1}/24:1(\text{OH}))\text{-H}]^-$ (m/z 904.6), $[\text{ST}(\text{d18:1}/24:1)\text{-H}]^-$ (m/z 888.6) and $[\text{ST}(\text{d18:1}/22:0)\text{-H}]^-$ (m/z 862.6). The ion at m/z 806 appeared as mixture of $[\text{PS}(16:0}/22:6)\text{-H}]^-$ and $[\text{ST}(\text{d18:1}/18:0)\text{-H}]^-$. Interestingly, this ion also showed some enrichment in AreaX, RA and TeO providing evidence for the presence of an additional DHA containing lipid, PS (16:0/22:6) within these regions. Ion images for m/z 862.6 and 888.6 are provided in Figure 2 h and i, respectively. The laminae have been observed with myelin staining³⁹ and thus the high concentration of sulfatides can be explained by their typically high abundance of in myelin. Myelin is also known to be rich in structurally-related galactosylceramides and upon close examination of the positive ion data several low intensity peaks at m/z 848 and 832, having mass defects ~ 0.1 Da higher than that typically observed for

phospholipids were identified and are tentatively assigned as the potassium and sodium adducts of the galactosylceramide (d18:1/24:1) (Supporting Information Figure S6). These ions are observed in the positive component 1 loadings spectra (Supporting Information Figure S1). This component reveals a related distribution but with some laminae not as clearly observed regions, possibly due to the low abundance of many of the myelin-specific ions in the positive ion mode. This highlights the additional biochemical and spatial information that is obtained by dual-polarity MSI.

Lipid Imaging of the Tumor Microenvironment

In cancer research the capability to image the molecular microenvironment of tumours is essential to both fundamental understanding of the processes that drive tumour biology, and preclinical and clinical procedures including drug discovery, and oncology diagnostics. Considering the essential roles of lipids in cell function, proliferation, differentiation and apoptosis,⁴⁰⁻⁴⁴ lipids are intimately involved in tumor biology. MSI can provide valuable information regarding the intratumour pathways involved in the formation, preservation and progression of the microenvironment. To better visualise lipid changes within the tumor microenvironment we have also employed dual-polarity MALDI-MSI to rapidly image changes in lipid distribution and composition within 5 sections from 4 different lung cancer xenograft tumours.

The full MS spectra in both polarities acquired from each xenograft are shown in Figure 3. Manual interrogation of the positive mode MSI datasets revealed the largest differences between xenograft 3 and the remaining 4 xenografts. Examination of this xenograft in the optical image from H&E staining showed that this is the only xenograft out of the five that did not contain a clear area of necrosis and this was supported by the MSI data. For example, m/z 725 in positive ion mode, identified as $[SM(d18:1/16:0)+Na]^+$ from MS/MS (See Supporting Information) strongly correlated with the regions of necrosis and revealed significantly lower abundance in xenograft 3, consistent with previous reports using a MDA-MB-231-tdTomato breast cancer model.⁴⁵

Figure 3 f and g show overlay images of 3 different m/z values that reveal different spatial distributions as observed in the negative and positive ion mode MSI data, respectively. In the negative ion mode few lipid-related signals were observed from the necrotic regions (see also Figures 4 and 5). However, strong signals were observed from the viable and regions adjacent

to the necrotic regions. The selected ions shown at m/z 861.5 (red), 766.5 (blue) and 913.5 (green) all reveal different spatial distributions throughout the viable tissue, a reflection of the underlying tissue heterogeneity. MS/MS data identified the strongest lipid contributor to these signals as the $[M-H]^-$ ions of PI(40:4) containing a 22:4 and 18:0 fatty acid, PE(38:4) containing an 18:0 and 20:4 fatty acid and PI (36:2) containing an 18:0 and 18:2 fatty acid, respectively (MS/MS spectra are provided as Supporting Information)). It should be noted that the MS/MS spectra in many cases reveal contributions from isomeric and isobaric lipids, suggesting the lipid compositions are much more complex than revealed by the ToF-MSI data. In addition, a variety of other lipid classes such as PE, PS, and PG were also observed in negative ion mode. Figure 3g shows an overlay of m/z 808.6 (red), 732.6 (blue) and 725.6 (green) observed in positive ion mode. The dominant lipids contributing to these ion signals were assigned as sodiated PC(36:2), protonated PC (32:1) and sodiated SM (18:1/16:0) based on the acquired on tissue MS/MS spectra (see Supporting Information Figure). The ion image of m/z 808.6 reveals it to be primarily distributed around the edges of the necrotic region while m/z 732.6 is mostly observed in the viable tissue.

To further investigate the underlying spatial features within the MSI datasets, both positive and negative ion data was subjected to multivariate image segmentation using pLSA. The individual component images and their loadings spectra are provided in the Supporting Information (Figure S7 and S8). Many components appeared to map to histologically different tissue regions as observed upon correlation with the H&E stained optical image (Supporting Information Figure S9). Component 1 in the positive ion dataset correlated strongly with the regions of necrosis in all xenografts. The underlying loading spectrum reveals the peaks contributing to this spatial distribution and many of these were confirmed upon visualisation of the single ion images. For example ions at m/z 725, 742, 768 and 835 were almost exclusively observed in the necrotic tissue and assigned as $[SM(d18:1/16:0)+Na]^+$ (m/z 725),

[PC(*O*-34:1)+Na]⁺ (*m/z* 768) and [SM(d18:1/24:1)+Na]⁺ (*m/z* 835), respectively. The ion at *m/z* 742 is assigned as both ¹³C isotope of the potassiated adduct of SM(d18:1/16:0) and [PC(*O*-32:0)+Na]⁺ based on the observation of a neutral loss of 205 Da (sodium phosphocholine), confirming the presence of a sodium adducted PC. That xenograft 3 did not show a significant contribution to positive ion component 1 provides further molecular evidence for the absence of necrosis in xenograft 3. Interestingly sodium adducted lipids dominated the spectra from the necrotic tissue, whereas protonated ions were primarily observed from the remaining tissue areas. We hypothesize this is due to the release of salts and other cellular material during necrosis that is then available for adduct formation during MALDI. Positive ion components 4, 8 and 10 also appeared to correlate with necrotic or near-necrotic regions. Each of these appeared correlated with a specific tissue structure revealed by the H&E image from a representative tissue region. The final four tissue-related components correlate to non-necrotic/viable regions which, although clearly molecularly distinct, are not readily distinguished from each other in the H&E staining. The microenvironmental heterogeneity described in these components may indicate more subtle cell processes within the tissue. Analysis of the corresponding negative ion data revealed many different spatial patterns in the MSI data. While little-to-no lipid signal was observed from the strongly necrotic regions as observed in positive ion mode, many distributions outside of the necrotic tissue were observed in the negative mode.

To evaluate the complementarity between the two data sets, we calculated Pearson correlation coefficients between the negative and positive component images (data not shown). With this approach it is possible to quantify the degree of linear correlation between two variables X (negative ion component) and Y (positive ion component), and thus provide a measure of similarity between the positive and negative ion MSI data. The coefficient ranges from +1 (strongly correlated, very similar) to -1 (totally anti-correlated), where 0 is no correlation (no

similarity). This method has been used as standard in MSI to calculate the similarity between a pair of MSI images.⁴⁶ Using Pearson correlation coefficients the strongest spatial correlations components relating to on-tissue features were observed between positive component 10 and negative component 2 (coefficient=0.75), positive components 10 and 6 with negative component 2 (0.75 and 0.77), and positive component 7 with negative component 5 (0.67) The remaining component pairs revealed lower correlation values (<0.5), demonstrating the different features that can be observed from the MSI data when both positive and negative ion data is acquired from the same tissue.

Finally, to make most use of the extra biochemical information within the combined polarity datasets we developed a combined pLSA model that incorporated both the positive and negative ion data into a single classification. This approach facilitates direct correlation of positive and negation ion lipids that contribute to the pLSA-revealed spatial features. The full combined pLSA component images are provided in the Supporting Information (Figure S10). Figure 4 shows several of these combined component images alongside optical images of the H&E stained section from regions appearing to overlay with the specific component. These demonstrate that the dual-polarity component images reveal many features that correspond to histologically distinct tissue regions across multiple tissues while simultaneously providing greater lipidome coverage than possible using a single polarity alone. For example combined components 3 and 6 appear correlated with the viable tissue regions. Component 7 is correlated with the tissue adjacent to the necrotic regions. It is possible this is tissue that is undergoing early necrosis. Component 9 is characterized as pre-necrotic with an increased presence of tumour stroma and some apoptotic nuclei while component 10 is directly correlated with the necrotic regions. Importantly xenografts 1 and 2 which are adjacent sections from the same animal give rise to very similar pLSA features demonstrating the technical reproducibility of the classification. A key advantage of this combined dual-polarity

approach is that the corresponding loadings spectra reveal, not only spectral features within a certain polarity that contribute to a particular spatial distribution, but also correlations *between* polarities allowing the relationships of all phospholipid classes to be revealed in a single analysis from the same tissue (Figure 5 and Supporting Information Figure S10). As an example, using the dual polarity loadings observed for the viable tissue in combined component 6 the abundant ion signals at m/z 742.6, 788.6, 863.6, 775.5, and 915.6 in negative mode are revealed to be related to the presence of m/z 760.5, 788.5, 798.5, 732.5, 826.5 and 808.5 in positive ion mode. These peaks have been identified in negative ion mode as (predominantly) the [M-H]⁻ ions of PE 36:2; PS 36:1; and PI 36:1; PG 36:1; and PI 40:3, respectively. In positive ion mode, peaks were identified as phosphocholine species; PC(34:1+H)⁺, PC(36:1+H)⁺, PC(34:1+K)⁺, PC(32:1+H)⁺, PC(36:1+K)⁺ and PC(36:2+Na)⁺, respectively. Such analytical approaches therefore enable the spatial correlation of a variety of lipid classes to be revealed in a single analysis, including, in this case PE, PS, PI and PC, and saturated and unsaturated fatty acid structures. This combined approach thus provides the research with a deeper understanding of changes occurring in the lipidome and the spatial correlations amongst different lipid classes not all observed in a single polarity alone.

Conclusions

In this work we have explicitly demonstrated the added biochemical and spatial information acquired when imaging tissue sections in both positive and negative mode using high-speed MALDI-MSI. Using norharamane as the MALDI matrix not only does each polarity provide complementary lipidomic coverage but each can reveal different spatial features within the MSI data. To take full advantage of the data produced by dual-polarity imaging from single sections we have developed a combined pLSA-based image segmentation approach that combines data acquired from each pixel in both polarity modes into a single image classification model. In applying this approach to investigating the spatial lipidomics changes within lung cancer xenografts we have shown that not only does the combined polarity classification model allow identification of chemically and histologically different tissue regions, but also the correlations between the highly complementary positive and negative lipid ion signals and their relationships to particular spatial features within the data can be directly revealed. Such approaches provide powerful analytical approaches for biomarker discovery, and open up the possibilities of correlating lipid MSI data to lipid pathways due to the greater lipidomics coverage and spatial correlations revealed. Combined with the rapid acquisition speed now possible with such instruments,^{23, 47} such dual polarity data analysis approaches provide a powerful and rapid tool to the lipidomics community that can now be fully exploited.

Acknowledgments

This research has been made possible with the support of the Dutch Province of Limburg. We acknowledge the support of Astra Zeneca for supplying tumor samples and for the financial support of J. C. N.O.P acknowledges support from FP7 European Union Marie Curie IAPP

Program, BRAINPATH. J. J and A. v. d. L acknowledge support from the Belgian Federal Science Policy Office through the grant P7/17. We are very thankful for the excellent ongoing technical support provided by Michael Becker, Jens Höhndorf, Christoph Nordmann, Marc Prihs and Arne Fuetterer of Bruker in Bremen.

References

1. M. R. Wenk, *Cell*, 2010, **143**, 888-895.
2. M. R. Wenk, *Nat Rev Drug Discov*, 2005, **4**, 594-610.
3. G. W. Feigenson, G. van Meer and D. R. Voelker, *Nature Reviews Molecular Cell Biology*, 2008, **9**, 112-124.
4. G. van Meer, *The EMBO Journal*, 2005, **24**, 3159-3165.
5. S. J. Blanksby and T. W. Mitchell, *Annual Review of Analytical Chemistry*, 2010, **3**, 433-465.
6. S. R. Ellis, S. H. Brown, M. in het Panhuis, S. J. Blanksby and T. W. Mitchell, *Prog. Lipid Res.*, 2013, **52**, 329-353.
7. K. A. Zemski Berry, J. A. Hankin, R. M. Barkley, J. M. Spraggins, R. M. Caprioli and R. C. Murphy, *Chem. Rev.*, 2011, **111**, 6491-6512.
8. C. Wu, A. L. Dill, L. S. Eberlin, R. G. Cooks and D. R. Ifa, *Mass Spectrom. Rev.*, 2012, n/a-n/a.
9. D. Gode and D. A. Volmer, *Analyst*, 2013, **138**, 1289-1315.
10. M. K. Passarelli and N. Winograd, *Biochim Biophys Acta Mol Cell Biol Lipids*, 2011, **1811**, 976-990.
11. E. E. Jones, T. W. Powers, B. A. Neely, L. H. Cazares, D. A. Troyer, A. S. Parker and R. R. Drake, *Proteomics*, 2014, **14**, 924-935.
12. L. Jiang, K. Chughtai, S. O. Purvine, Z. M. Bhujwalla, V. Raman, L. Paša-Tolić, R. M. A. Heeren and K. Glunde, *Anal. Chem.*, 2015, **87**, 5947-5956.
13. R. Mirnezami, K. Spagou, P. A. Vorkas, M. R. Lewis, J. Kinross, E. Want, H. Shion, R. D. Goldin, A. Darzi, Z. Takats, E. Holmes, O. Cloarec and J. K. Nicholson, *Molecular Oncology*, 2014, **8**, 39-49.
14. M. T. Villanueva, *Nat Rev Cancer*, 2014, **14**, 706-706.
15. S. Guenther, L. J. Muirhead, A. V. M. Speller, O. Golf, N. Strittmatter, R. Ramakrishnan, R. D. Goldin, E. Jones, K. Veselkov, J. Nicholson, A. Darzi and Z. Takats, *Cancer Res.*, 2015, **75**, 1828-1837.
16. L. S. Eberlin, I. Norton, A. L. Dill, A. J. Golby, K. L. Ligon, S. Santagata, R. G. Cooks and N. Y. R. Agar, *Cancer Res.*, 2012, **72**, 645-654.
17. D. Calligaris, D. Caragacianu, X. Liu, I. Norton, C. J. Thompson, A. L. Richardson, M. Golshan, M. L. Easterling, S. Santagata, D. A. Dillon, F. A. Jolesz and N. Y. R. Agar, *Proc. Natl. Acad. Sci.*, 2014, **111**, 15184-15189.
18. A. D. Feenstra, R. L. Hansen and Y. J. Lee, *Analyst*, 2015, **140**, 7293-7304.
19. S. Guo, Y. Wang, D. Zhou and Z. Li, *Scientific Reports*, 2014, **4**, 5959.
20. M. Nazari and D. C. Muddiman, *Analyst*, 2016, **141**, 595-605.
21. A. Korte and Y. Lee, *J. Am. Soc. Mass. Spectrom.*, 2013, **24**, 949-955.
22. A. Thomas, J. L. Charbonneau, E. Fournaise and P. Chaurand, *Anal. Chem.*, 2012, **84**, 2048-2054.
23. N. Ogrinc Potočnik, T. Porta, M. Becker, R. M. A. Heeren and S. R. Ellis, *Rapid Commun. Mass Spectrom.*, 2015, **29**, 2195-2203.
24. A. Thomas, N. H. Patterson, M. M. Marcinkiewicz, A. Lazaris, P. Metrakos and P. Chaurand, *Anal. Chem.*, 2013, **85**, 2860-2866.
25. T. Schramm, A. Hester, I. Klinkert, J.-P. Both, R. M. A. Heeren, A. Brunelle, O. Laprévotte, N. Desbenoit, M.-F. Robbe, M. Stoeckli, B. Spengler and A. Römpf, *J. Proteomics*, 2012, **75**, 5106-5110.
26. M. Hanselmann, M. Kirchner, B. Y. Renard, E. R. Amstalden, K. Glunde, R. M. A. Heeren and F. A. Hamprecht, *Anal. Chem.*, 2008, **80**, 9649-9658.
27. E. A. Brenowitz, D. Margoliash and K. W. Nordeen, *J. Neurobiol.*, 1997, **33**, 495-500.
28. J. M. George, H. Jin, W. S. Woods and D. F. Clayton, *Neuron*, 1995, **15**, 361-372.
29. N. I. Denisenko-Nehrbass, E. Jarvis, C. Scharff, F. Nottebohm and C. V. Mello, *Neuron*, 2000, **27**, 359-370.

30. J. K. Jeong, T. A. F. Velho and C. V. Mello, *The Journal of Comparative Neurology*, 2005, **489**, 23-41.
31. K. Soderstrom, Q. Y. Tian, M. Valenti and V. Di Marzo, *J. Neurosci.*, 2004, **24**, 10013-10021.
32. K. R. Amaya, J. V. Sweedler and D. F. Clayton, *J. Neurochem.*, 2011, **118**, 499-511.
33. K. R. Amaya, E. B. Monroe, J. V. Sweedler and D. F. Clayton, *Int. J. Mass. Spectrom.*, 2007, **260**, 121-127.
34. J. H. Stoner and R. Rushfield, *Conservation of Easel Paintings*, Taylor & Francis, New York, 2012.
35. G. Silvester, A. Burnstock, L. Megens, T. Learner, G. Chiari and K. J. van den Berg, *Stud. Conserv.*, 2014, **59**, 38-51.
36. v. d. K. J. Berg, A. Burnstock, M. de Keijzer, J. Krueger, T. Learner, d. A. Tagle and G. Heydenreich, *The Interface Between Science and Conservation and the Challenges for Modern Oil Paint Research*, Springer International Publishing, Switzerland, 2014.
37. M. I. Gurr, J. L. Harwood and K. N. Fraym, *Lipid Biochemistry An Introduction*, 5th edn., Blackwell Science, Oxford, 2002.
38. *Modern paints uncovered : proceedings from the modern paints uncovered symposium*, Los Angeles, Getty Conservation Institute, 2007.
39. H. J. Karten, A. Brzozowska-Prechtel, P. V. Lovell, D. D. Tang, C. V. Mello, H. Wang and P. P. Mitra, *J. Comp. Neurol.*, 2013, **521**, 3702-3715.
40. M. Verheij, R. Bose, X. H. Lin, B. Yao and et al., *Nature*, 1996, **380**, 75-79.
41. Y. Li, P. Maher and D. Schubert, *Proc. Natl. Acad. Sci.*, 1998, **95**, 7748-7753.
42. Q. Zhang and M. J. O. Wakelam, *Advances in Biological Regulation*, 2014, **54**, 93-98.
43. S. Ran and P. E. Thorpe, *International Journal of Radiation Oncology*Biophysics*, 2002, **54**, 1479-1484.
44. A. Lucci, W. I. Cho, T. Y. Han, A. E. Giuliano, D. L. Morton and M. C. Cabot, *Anticancer Res.*, 1998, **18**, 475-480.
45. K. Chughtai, L. Jiang, T. R. Greenwood, K. Glunde and R. M. A. Heeren, *J. Lipid Res.*, 2013, **54**, 333-344.
46. T. Alexandrov, *BMC Bioinformatics*, 2012, **13**, (Suppl 16):S11.
47. J. Spraggins and R. Caprioli, *J. Am. Soc. Mass. Spectrom.*, 2011, **22**, 1022-1031.

Figures

Figure 1

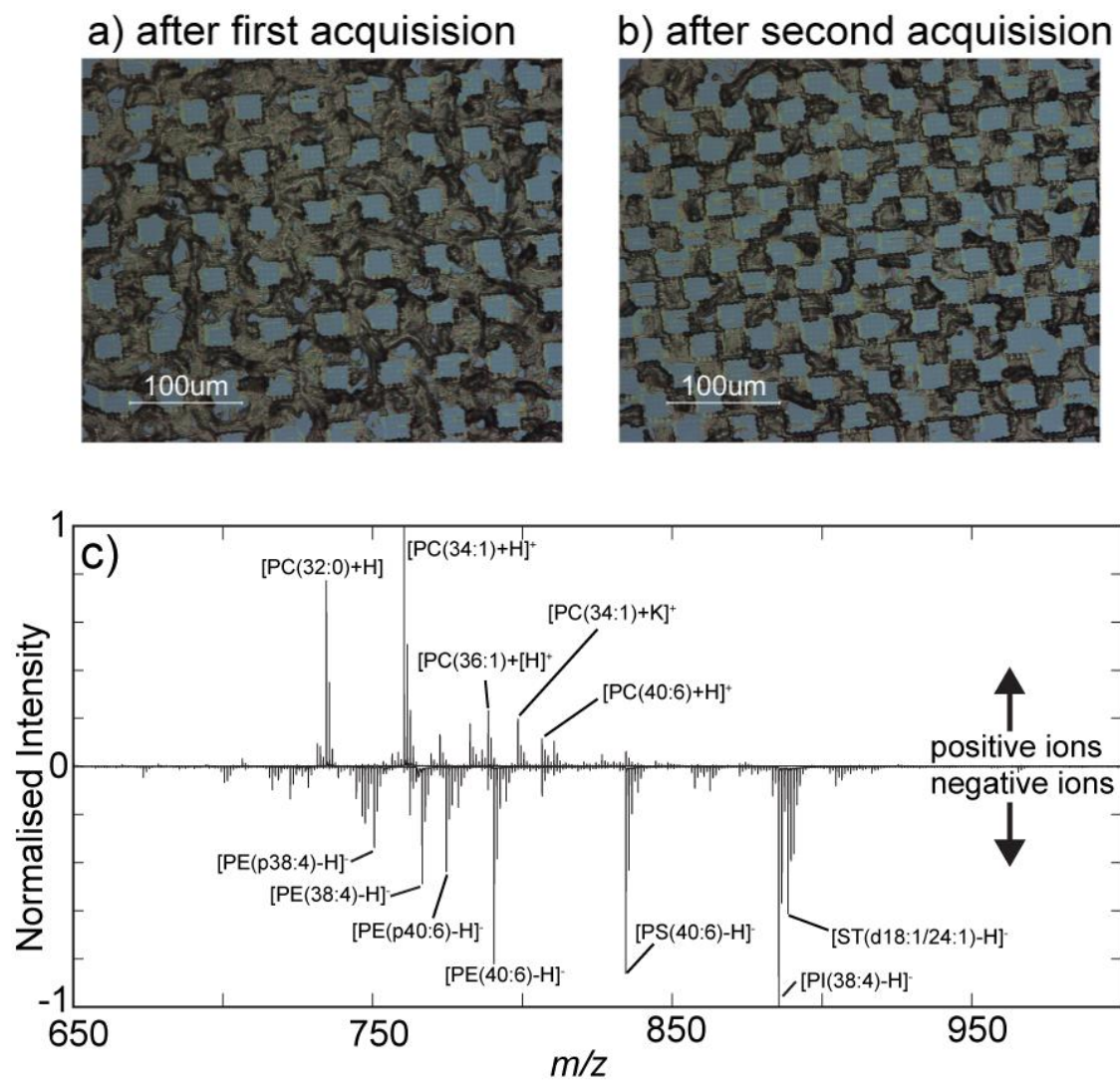


Figure 2

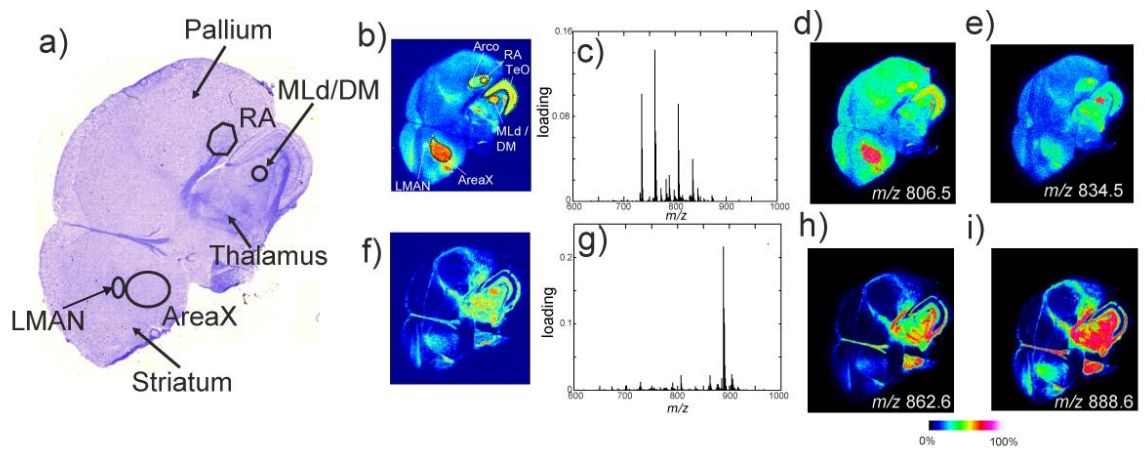


Figure 3

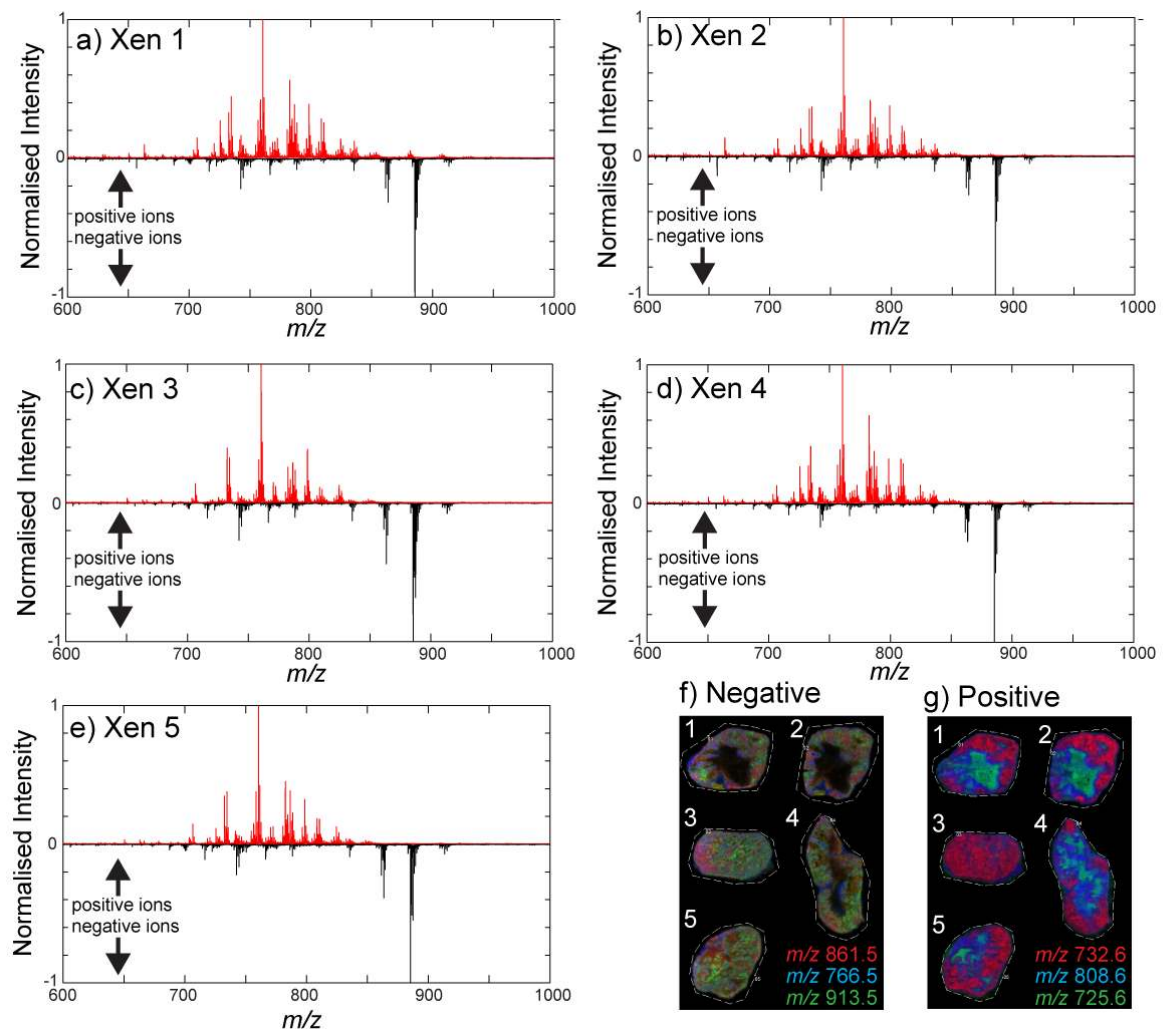


Figure 4

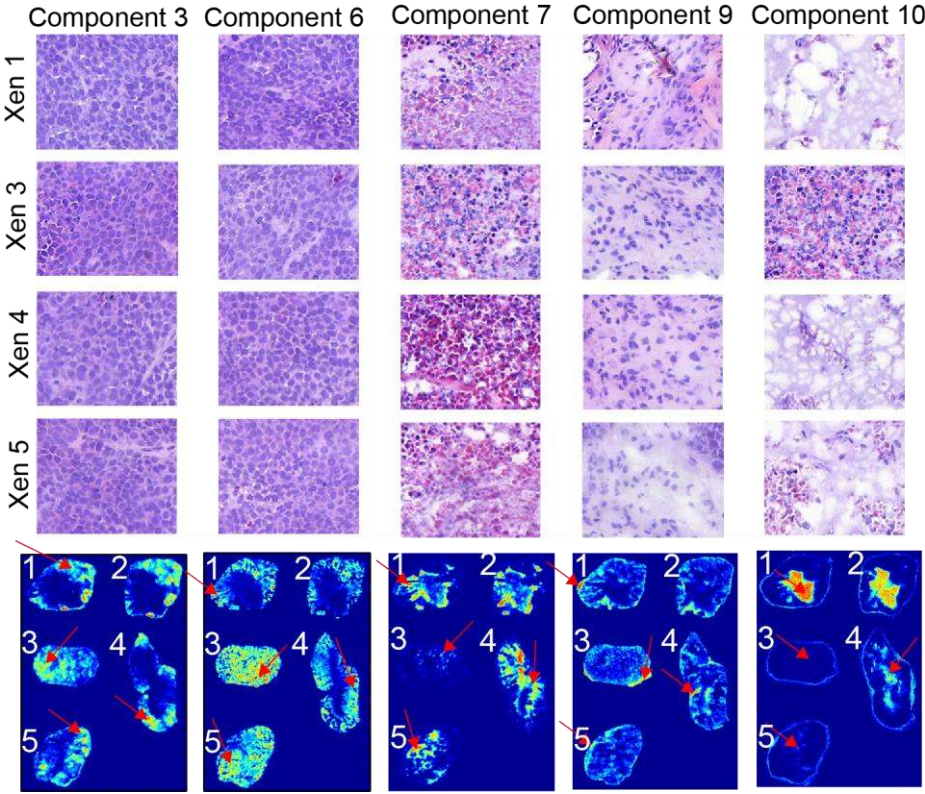


Figure 5

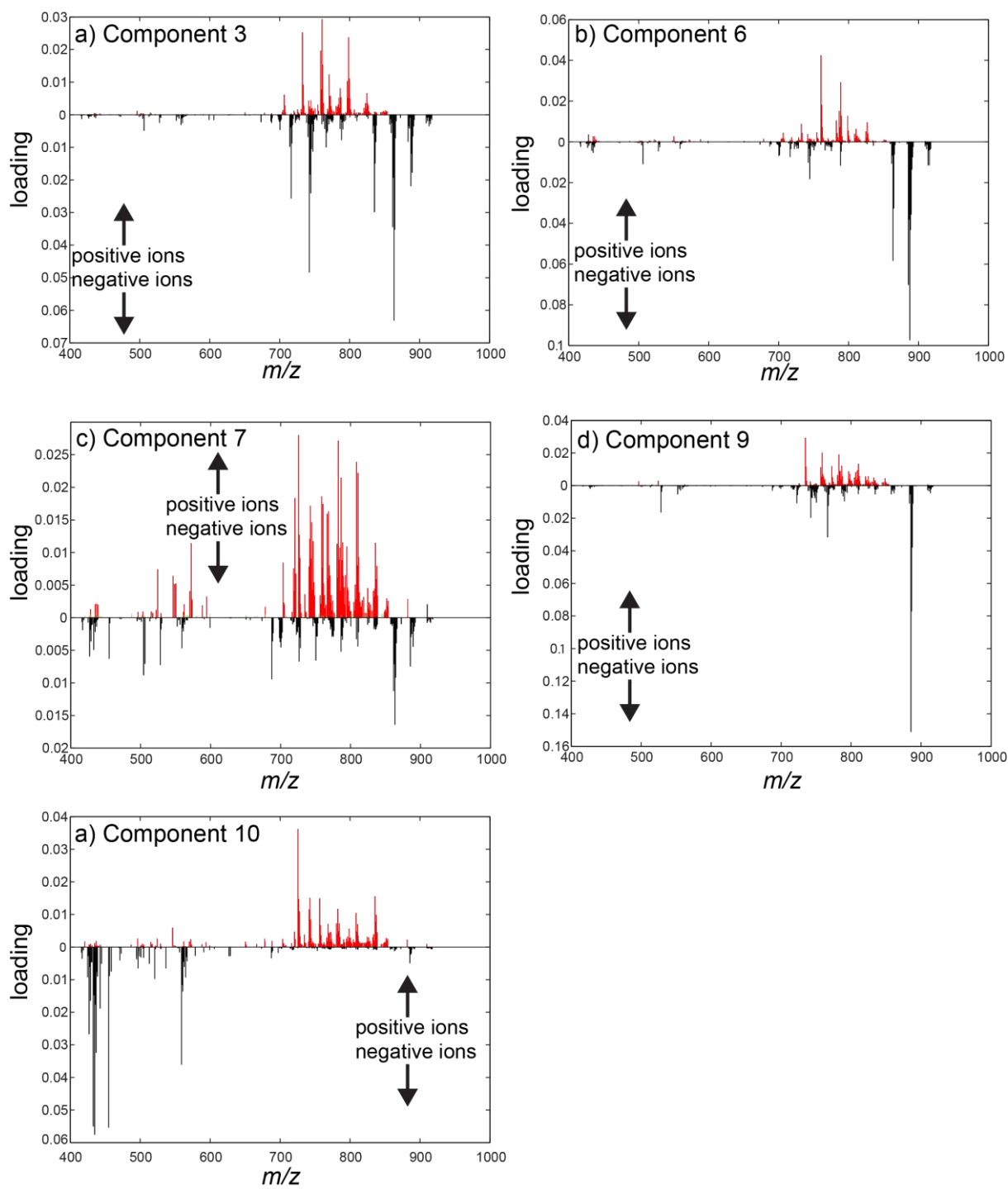


Figure Captions

Figure 1. (a) Optical image of norharmane matrix deposited onto an ITO slide and after laser desorption using a $20 \times 20 \mu\text{m}^2$ beam scan and a $50 \times 50 \mu\text{m}^2$ raster. (b) Optical image of norharmane matrix after a laser desorption step using identical parameters as (a) except with a $25 \times 25 \mu\text{m}^2$ stage offset applied for the second acquisition. Note for illustration purposes data was acquired with more laser shots and laser energy than typically used for MSI acquisitions. (c) Average positive and negative ion spectra acquired across a zebra finch brain section using norharmane matrix.

Figure 2. (a) Optical image of cresyl violet stained zebra finch section with key regions labelled. (b) Positive ion pLSA component 4 image. (c) Positive ion pLSA component 4 loadings spectrum. (d) and (e) Selected positive ion images of m/z 806.5 ([PC (16:0/22:6+H)]⁺) and 834.5 ([PC (18:0/22:6+H)]⁺). (f) Negative ion pLSA component 3 image. (g) Negative ion pLSA component 4 loadings spectrum. (h) and (i) Selected negative ion image of m/z 862.6 ([ST(d18:1/22:0)-H]⁻) and 888.6 ([ST(d18:1/24:1)-H]⁻).

Figure 3. (a)-(e) Integrated positive and negative ion spectra acquired from each tumor xenograft. (f) Negative ion overlay image showing m/z 861.5 (red), m/z 766.5 (blue) and m/z 913.5 (green) within the xenograft sections. (g) Positive ion overlay image showing m/z 808.6 (red), m/z 732.6 (blue) and m/z 725.6 (green) within the xenograft sections. Sections one and two are replicates from the same xenograft

Figure 4. 5 selected pLSA component images generated from the combined positive and negative ion dataset. Components correlate with histologically different tissue regions. Above each pLSA image are enlarged images of the H&E stained section from different xenografts that correspond in location to the regions indicated by the red arrows. Sections one and two are replicates from the same xenograft

Figure 5. pLSA loadings spectra produced from the combined positive and negative ion mode dataset and corresponding to the images shown in Figure 4. Positive ion contributions are shown in red and negative ion contributions shown in black. Such analyses allow direct correlation of positive and negative ion lipid data to spatial features revealed by pLSA.